

General Disclaimer

One or more of the Following Statements may affect this Document

- This document has been reproduced from the best copy furnished by the organizational source. It is being released in the interest of making available as much information as possible.
- This document may contain data, which exceeds the sheet parameters. It was furnished in this condition by the organizational source and is the best copy available.
- This document may contain tone-on-tone or color graphs, charts and/or pictures, which have been reproduced in black and white.
- This document is paginated as submitted by the original source.
- Portions of this document are not fully legible due to the historical nature of some of the material. However, it is the best reproduction available from the original submission.

DRA

PLANETARY ASTRONOMY
PROGRAM

Second Quarterly Report
15 February 1976

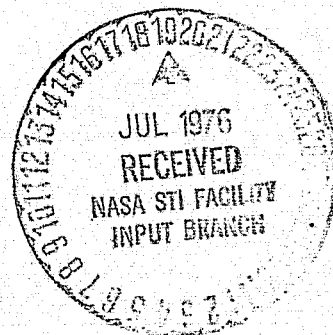
(NASA-CR-148460) PLANETARY ASTRONOMY
PROGRAM (Planetary Science Inst., Tucson,
Ariz.) 62 p HC \$4.50 CSCI 03A

N76-29083

Unclas
G3/89 15221

Submitted by:

Planetary Science Institute
2030 East Speedway, Suite 201
Tucson, Arizona 85719



**TASK 1: SPECTROPHOTOMETRIC OBSERVATIONS AND
ANALYSIS OF THE ASTEROIDS**

(Principal Investigator: Clark R. Chapman)

Work on this task proceeded at a somewhat reduced pace this quarter inasmuch as no asteroid observing runs were scheduled. Most effort was devoted to reduction and interpretation of data and preparation for presentation at forthcoming meetings.

The observational program will get under way again in May. Time has been assigned for visible and near-IR spectrophotometry by Chapman and McCord at the Kitt Peak National Observatory for early May when efforts will be made to secure observations of Betulia and other important asteroids.

Data reduction has been proceeding on observations obtained earlier in 1975 intended for presentation at forthcoming meetings, including the Division for Planetary Sciences of the AAS meeting in Austin, Texas, in early April.

Chapman has been working with a group of other asteroid researchers, including Morrison, Gehrels, Williams, and Zellner, to establish a computerized data file of physical observations of asteroids. It is intended that efficient use of this file will permit a wide variety of statistical and analytical studies to be performed later in the spring, in preparation for the I.A.U. Colloquium, scheduled for mid-August in Lyon.

Preparations for an intensive observational campaign in support of a possible fly-by of asteroid 92 Undina by the Mariner Jupiter-Saturn mission have been suspended. Further calculations at J.P.L. have revealed that the pass will not be sufficiently close to Undina to permit useful observations.

The text of the asteroid review article by Hartmann, Chapman, and Williams has been finished and the manuscript has been circulated to several other asteroid experts for review. The manuscript will be submitted to Space Science Reviews, which issued the original invitation for the review, within a month or so.

It is intended that the next quarter will see the conclusion of reduction and analysis of previous spectrophotometry.

TASK 2: LUNAR OCCULTATION OF ASTEROIDS

(Principal Investigator: Donald R. Davis)

This task is scheduled for the third quarter of the contract year and no work was performed nor any funds expended during the second quarter.

**ORIGINAL PAGE IS
OF POOR QUALITY**

TASK 3: ANALYSIS OF SATURN'S RINGS

(Principal Investigator: M. J. Price)

Visual photometric function data for Saturn's rings have been analyzed in terms of elementary anisotropic scattering radiative transfer models which involve the Henyey-Greenstein function. Limits have been placed on the combinations of single scattering albedo, and back-scattering directivity, which are permitted by observation. Particles with lunar-like scattering properties are excluded by the analysis. Results are consistent with the ring particles being more-or-less pure, and spherical, conglomerates of H₂O frost. Details of the analysis are contained in a paper entitled "Anisotropic Optical Scattering Within Saturn's Rings" which is in preparation for publication in Icarus. A draft is reproduced in Appendix A.

Determining the degree of contamination of the "snowball" particles remains a problem yet to be solved. Work is now progressing in this area based on unpublished laboratory photometric data by Veverka (1976, Private Communication). Using powdered mixtures of magnesium oxide and charcoal, Veverka has attempted to simulate the effects of mineral contamination on snow. For pure MgO surfaces, laboratory measurements both of the geometrical albedo, and of the phase integral, agree well with earlier studies of natural snow. Comparison of the laboratory studies with the photometric analysis of the rings is still in progress. Results will be factored into the final version of the paper. It appears likely that mineral contamination of the ring particles cannot exceed 5 percent by weight.

Co-investigator W. K. Hartmann has obtained films of collisional effects between icy particles, involving collision velocities from about 10^2 to 10^4 cm/sec. Images reveal rebound velocities, size distributions of fragments, and possibly rotational characteristics in free fall, applicable to Saturn's rings. Analysis has not yet begun.

ORIGINAL PAGE IS
OF POOR QUALITY.

TASK 4: PROBING THE URANUS ATMOSPHERE WITH THE RAMAN EFFECT

(Principal Investigator: M. J. Price)

During the current reporting period, emphasis was placed on the Saturn task. Consequently, work on Uranus progressed only slowly. Even so, several significant accomplishments deserve to be reported.

First, computation of the strengths of the rotational Raman ghost images of Fraunhofer features in the Uranus spectrum is progressing satisfactorily. Isotropic scattering in an H_2 gaseous layer about a Lambert cloud layer is being assumed. Emphasis is being placed on single scattering albedos ~ 0.95 , and an optical thickness in the range $0 \leq \tau \leq 3$.

Second, exploratory observations will be carried out in collaboration with Dr. Michael J. S. Belton during April using a Fourier Transform Spectrometer in conjunction with the McMath Solar Telescope. Rotational Raman ghost images will be studied at blue ($\lambda 4000\text{\AA}$) and yellow (5500\AA) wavelengths to determine if their strengths are wavelength dependent. Such a dependence can be explained in terms of a cloud layer underlying a Rayleigh scattering H_2 atmosphere. The depth of the cloud layer can be inferred.

Third, complementary studies of the limb-brightening phenomenon on the Uranus disk are progressing well. Results of the collaborative investigation with Dr. Otto Franz up until the end of the 1975 observing season are contained in a paper entitled "Limb-Brightening on Uranus: The Visible Spectrum," recently accepted for publication in Icarus. A copy is contained in Appendix B.

Fourth, new limb-brightening observations were secured within the last two weeks at Lowell Observatory by Dr. Franz. Limb-brightening is very obvious in the $\lambda 7300$ CH_4 band. By replacing the original EMI 9558 photomultiplier with a red-sensitive RCA tube, the signal-to-noise ratio has been increased by a factor 3. By refiguring the Cassegrain Secondary of the 72-inch Perkins reflector to eliminate residual spherical aberration, Loomis (University of Arizona, Optical Sciences Center) has reduced the half-width of the point spread function by a factor 2, a truly astonishing feat. The PSF half-width is now typically $\sim 1''$ arc or less. Limb-brightening has become correspondingly easier to detect. As more data accumulate during the 1976 observing season, we expect to be able to address the question of the aerosol particle distribution in the Uranus atmosphere. These studies can then be factored into development of the Raman probe technique.

TASK 5: FOLLOW-ON STUDIES OF MARS DATA COLLECTIONS

(Principal Investigator: William K. Hartmann)

Material from preceding year's studies, together with some recently published related material, has been collected for final processing to produce a publication. Final manuscript is not yet complete.

ORIGINAL PAGE IS
OF POOR QUALITY

APPENDIX A

ANISOTROPIC
OPTICAL SCATTERING
WITHIN
SATURN'S RINGS

by

Michael J. Price
Planetary Science Institute
Tucson, Arizona 85719

Received _____

Revised _____

No. of Copies: 4

No. of MS Pages: 24

No. of Figures: 5

No. of Tables: 1

Proposed Running Head:

ANISOTROPIC OPTICAL SCATTERING

Name and Address to Whom Proofs Should Be Sent:

Dr. Michael J. Price

Planetary Science Institute

2030 E. Speedway Blvd., Suite 201

Tucson, Arizona 85719

ORIGINAL PAGE IS
OF POOR QUALITY

ABSTRACT

Visual photometric function data for Saturn's rings are analyzed in terms of elementary anisotropic scattering radiative transfer models which involve the Henyey-Greenstein function. Limits are placed on the combinations of single scattering albedo, and back-scattering directivity, which are permitted by observation. Particles with lunar-like scattering properties are excluded by the analysis. Results are consistent with the ring particles being more-or-less pure, and spherical, conglomerates of H_2O frost.

ORIGINAL PAGE IS
OF POOR QUALITY

I. INTRODUCTION

Some time ago, Price (1973, 1974) rediscussed the optical scattering properties of Saturn's rings. Evidence indicating that the photometric function at visual wavelengths is dominated by primary scattering, and that mutual shadowing is an irrelevant concept, was first presented. Available ground-based photometric data were then interpreted on the basis of simple radiative transfer models. Only moderate degrees of anisotropic scattering were treated. Special attention was given to the case of individual, spherical, macroscopic particles for which the scattering phase function is proportional to the apparent area illuminated. More extreme cases of back-scattering were not considered. Probable ranges in the single scattering albedo, and in the general shape of the scattering phase function, were defined. Limitations on the mean perpendicular optical thickness of rings A and B together were also obtained. Results indicated that the ring particles are efficient back-scatterers of visual radiation. Isotropic scattering is not permitted. Based on an infinite optical thickness for the rings, a minimum single scattering albedo ~ 0.75 was found. Use of conservative scattering led to a minimum optical thickness ~ 0.7 .

Using elementary radiative transfer theory, based on the simple optical scattering model, Price (1976) recently analyzed the available infrared ($10\text{ }\mu\text{m}$ and $20\text{ }\mu\text{m}$) thermal emission data for Saturn's rings.

The ring system was treated as an isothermal slab of finite optical thickness. To obtain sufficient heating of the ring material, optical single scattering albedos less than 0.75 were required. Moreover, the rings could not be isothermal. To reconcile the results with the analysis of the photometric function, the back-scattering efficiency of each individual particle must be even higher than the maximum assumed. Higher back-scattering efficiencies permit lower single scattering albedos, and smaller optical thicknesses.

Further theoretical analysis of the visual photometric function data is contained in this paper. Emphasis is placed on fully defining the constraints on the single scattering albedo, and on the shape of the scattering phase function. Extreme degrees of anisotropy are treated. Scattering phase functions ranging from total back-scattering to isotropic scattering are considered.

ORIGINAL PAGE IS
OF POOR QUALITY.

II. THEORY

1. Primary Scattering: Its Role

Since previous studies (Price, 1973; 1974) have indicated that primary scattering dominates the visual photometric function, our analysis will be based on the theory of primary scattering; multiple scattering will be included as a perturbation only. Zero phase angle, where the rings appear wide open will be assumed. Both the insignificance of multiple scattering, and the geometry of the situation, exclude the application of the van de Hulst similarity principles.

Defining the radiative transfer model is our initial task. Following Price (1973; 1974), let us assume the ring system to be a plane-parallel layer of particles with an optical thickness, τ_0 . Each ring particle is described by its single scattering albedo, ω , and by its scattering phase function, $p(\Theta)$. For convenience, the scattering phase function is normalized, by integrating over all scattering angles, Θ , such that

$$\int p(\Theta) \frac{dw}{4\pi} = 1 \quad (1)$$

where the element of solid angle, dw , is the variable. Once again mutual shadowing is taken to be negligible. Interparticle separations are considered to be sufficiently large that radiation scattered by each particle is reliably described by the far field approximation.

Deriving a relationship between the specific intensity, resulting from single scattering alone, and the parameters of the radiative transfer model is our next task. For any chosen layer of the ring system, located between optical depth τ and $\tau + d\tau$, the primary scattering contribution, $dI^{(1)}(\tau)$, to the intensity of radiation diffusely reflected towards zero phase angle can be readily evaluated. Let the solar flux at Saturn be denoted πF . At an optical depth τ , the fraction $\exp(-\tau/\mu_0)$ of the incident flux arrives without having suffered any scattering process in the intervening medium. The μ_0 parameter is the cosine of the angle of incidence with respect to the outward normal to the ring system. The contribution to the diffuse intensity in the direction of zero phase angle at depth τ by this reduced incident flux is

$$\frac{1}{4} \cdot F \cdot e^{-\tau/\mu_0} \cdot \omega \cdot p(180^\circ) \cdot \frac{d\tau}{\mu} \quad (2)$$

where the μ parameter is the cosine of the angle of reflection with respect to the outward normal to the ring system. A fraction $\exp(-\tau/\mu)$ of this amount emerges in the zero phase direction without suffering any further scattering. Consequently, the contribution to the emergent intensity by light which has suffered a single scattering in the layer between τ and $\tau + d\tau$ is

$$dI^{(1)}(\tau) = \frac{1}{4} \cdot F \cdot e^{-\tau/\mu} \cdot e^{-\tau/\mu_0} \cdot \omega \cdot p(180^\circ) \cdot \frac{d\tau}{\mu} \quad (3)$$

The total contribution to the emergent intensity of light which has suffered only a single scattering within the ring system can be obtained by integrating equation (3) over all optical depths. We have

$$I^{(1)}(\mu, \mu_0, \tau_0) = \frac{1}{4} \cdot \omega \cdot F \cdot \frac{\mu_0}{(\mu + \mu_0)} \cdot p(180^\circ) \cdot \left\{ 1 - \exp\left[-\left(\frac{1}{\mu} + \frac{1}{\mu_0}\right)\tau_0\right] \right\} \quad (4)$$

Except when the ring system appears nearly edge-on to the sun and Earth, the angles of incidence and reflection are always nearly equal. For the geometrical situation of interest in this paper, we will adopt μ equal μ_0 equal 0.44124. Equation (4) can then be re-written

$$I^{(1)}(\mu_0, \tau_0) = \frac{1}{8} \cdot \omega \cdot F \cdot p(180^\circ) [1 - \exp(-2\tau_0/\mu_0)] \quad (5)$$

Equation (5) explicitly relates the specific intensity for primary back-scattering to the individual parameters of the radiative transfer model.

Multiple scattering can be treated through the ratio of primary-to-multiple scattering, f . Denoting the total specific intensity, I , we can re-write equation (5) as

$$I^{(1)}(\mu_0, \tau_0) = f \cdot I(\mu_0, \tau_0) = \frac{1}{8} \cdot \omega \cdot F \cdot p(180^\circ) [1 - \exp(-2\tau_0/\mu_0)] \quad (6)$$

which becomes

$$\frac{I(\mu_o, \tau_o)}{F} = \frac{1}{8} \cdot \omega \cdot \frac{1}{F} \cdot p(180^\circ) [1 - \exp(-2\tau_o/\mu_o)] \quad (7)$$

Equation (7) is the basis of our analysis. In principle, since $\frac{I}{F}(\mu_o, \tau_o)$ can be obtained directly from photometry of the ring system, tight constraints can be placed on the permissible combinations of radiative transfer parameters. In practice, two problems must first be addressed. The scattering phase function must be defined. In addition, the primary-to-multiple scattering ratio must be known adequately. Since the ratio is a function of the single scattering albedo, of the optical thickness, of the scattering phase function, and of the geometries of solar illumination and of ground-based observation, its evaluation requires careful consideration.

2. The Scattering Phase Function: The Choice

Selection of the scattering phase function must meet two requirements. First, its general shape must be described by a single parameter. Second, it must encompass all extremes. The Henyey-Greenstein (1941) function

$$p(\Theta) = \frac{(1 - g^2)}{(1 + g^2 - 2g \cos \Theta)^{3/2}} \quad (8)$$

ORIGINAL PAGE IS
OF POOR QUALITY

is the natural choice. General shape is described by the g parameter.

For zero phase angle, equation (8) may be written

$$p(180^\circ) = \frac{(1 - g)}{(1 + g)^2} . \quad (9)$$

Extreme shapes include isotropic scattering ($g = 0$), complete forward-scattering ($g = +1$), and complete back-scattering ($g = -1$).

3. Primary and Multiple Scattering: Their Ratio

Accurately determining the primary-to-multiple scattering ratio in a radiative transfer problem which includes an arbitrary Henyey-Greenstein phase function can be done only numerically. Nevertheless, the issue can be adequately sidestepped by utilizing known analytical solutions for radiative transfer problems which involve simpler scattering phase functions. Similar scattering phase functions imply similar radiative transfer solutions. Our analysis will assume that, rather than being similar, the solutions are in fact identical.

Chandrasekhar (1960) has extensively studied radiative transfer problems in which the scattering phase function is described by the expression

$$p(\Theta) = (1 + x \cos \Theta) , \quad -1 \leq x \leq +1 . \quad (10)$$

TABLE I

PRIMARY AND MULTIPLE SCATTERING: THEIR RATIO

(Zero Phase Angle; $\mu = \mu_0 = 0.44124$)

ω	$x = 0$				$x = -1$			
	$\tau = .1$	$\tau = .5$	$\tau = 1$	$\tau = \infty$	$\tau = .1$	$\tau = .5$	$\tau = 1$	$\tau = \infty$
.75	.879	.690	.614	.565	.955	.850	.796	.759

Two cases of special interest are isotropic scattering ($x = 0$) and moderate back-scattering ($x = -1$). Both special cases are compared with several Henyey-Greenstein functions in Fig. 1. Isotropic scattering is described exactly by setting either g or x equal to zero. Moderate back-scattering, represented by x equal to -1 , is well approximated by the Henyey-Greenstein function with g equal to -0.25 . For the case of complete back-scattering ($g = -1$), only primary scattering can occur ($f = 1$).

Primary-to-multiple scattering ratios have been calculated for a variety of ω , x , τ combinations by methods outlined by Price (1974). Results are listed in Table I. The values given are lower limits obtained by adopting the maximum permissible value (0.75) for the single scattering albedo; cf. Price (1976).

III. ANALYSIS

Determining the allowable ω -g envelope of ring particle parameters requires fundamental knowledge of the visual photometric function for the geometrical situation of interest. In rediscussing the observational data, Price (1974) showed that the relevant mean $\frac{I}{F}$ value, for rings A and B together, must lie in the range $0.25 \leq \frac{I}{F} \leq 0.4$. Knowledge of the mean optical thickness is important too. For a lower limit, the τ_0 value 0.1 will be adopted. Smaller optical thicknesses would imply that stars, and Saturn's disk, would be easily visible through ring B, a situation contrary to experience. Most probably, the mean optical thickness lies in the range $0.5 \leq \tau_0 \leq 2$; cf: Pollack (1975). In our present analysis, special attention will be given to optical thicknesses in the range $0.5 \leq \tau \leq \infty$.

Values for the single scattering albedo, ω , corresponding to definite choices for g , τ_0 , μ_0 , and f , can be readily obtained from equation (7), which for convenience can be re-written simply as

$$\omega = 8 \cdot \frac{I}{F} \cdot f \cdot \left\{ p(180^\circ) [1 - \exp(-2\tau_0/\mu_0)] \right\}^{-1}, \quad (11)$$

where $p(180^\circ)$ is given by equation (9). Once g , τ_0 , μ_0 are selected, the only weakness in the precise calculation of ω lies in uncertainties in the two parameters, $\frac{I}{F}$ and f . Extreme ω -values may be obtained by adopting extreme values for the latter.

Given g , τ_0 , μ_0 , the maximum and minimum permissible ω values are obtained when both $\frac{I}{F}$, f are maximized or minimized, respectively. From the observational data, the maximum and minimum $\frac{I}{F}$ values are 0.4 and 0.25, respectively. Obviously, the primary-to-multiple scattering ratio has a maximum value unity. Table I can provide suitable minimum estimates for the f -value. Isotropic scattering, an infinite optical thickness, and a single scattering albedo 0.75, together produce the absolute minimum f -value (0.565) which can be relevant to the Saturn ring problem. Fig. 2 illustrates the corresponding allowable, and non-allowable, ω - g envelopes for a number of relevant τ -ranges. Note that ω -values greater than 0.75 are excluded by infrared studies, cf: Price (1976).

Several conclusions can be drawn from Fig. 2. First, the observations constrain the single scattering albedo and the anisotropy parameter to be coupled. Large ω -values necessitate only minor anisotropy. By contrast, small ω -values require a high degree of anisotropy. Second, it is clear that the ring particles must be highly efficient back-scatterers of visual radiation, confirming earlier studies by Price (1973, 1974). Indeed, Fig. 2 suggests that the back-scattering directivity may be significantly more pronounced than for the special case (Fig. 1) of x equal -1. If so, then the lower limits, shown in Fig. 2, for the single scattering albedo for a given g -value are too.

small. In fact, the calculation of minimum ω -values should utilize the f -value which corresponds to the special case of moderate back-scattering ($x = -1$), infinite optical thickness, and a single scattering albedo 0.75. Table I shows the relevant primary-to-multiple scattering ratio to be 0.759. For constant g , the lower bounds to ω in Fig. 2 would be raised by a factor $0.759/0.565$ (1.34) at g equal -0.25. For g values approaching -1, the factor will increase to $1/0.565$ (1.77). Evidently, the back-scattering efficiency of the ring particles must indeed be greater than for the special case x equal -1.

IV. DISCUSSION

Current knowledge (Pollack, 1975) suggests that the ring particles are macroscopic pieces of H_2O -ice, with characteristic dimensions on the order of a few centimeters. Determining if the single scattering albedos and scattering phase functions characteristic of such particles are permitted by our analysis is important. Since knowledge of the surface texture, and general shape, of the ring particles does not exist, we will assume for convenience that they are smooth and spherical.

Recently, Veverka(1973) has studied the photometric properties of snow and of snow-covered planets. His results are directly applicable to the Saturn ring problem. Using measurements of natural snow surfaces as phase angles up to 80 degrees, Veverka concluded that in general snow is a quasi-Lambert scatterer, with a characteristic Minnaert constant, k , in the range $1.04 \leq k \leq 1.35$. Even in an extreme case of specular reflection (a "glazed rain mist"), k was less than 2 for the phase angles considered. In evaluating the scattering properties of snow-covered planets, Veverka derived Bond albedos, A_B , in the range $0.51 \leq A_B \leq 0.82$, with the most likely case $A_B > 0.67$.

Far-field scattering phase functions for snowballs have been derived for two values of the Minnaert constant, k , viz., k equal 1 and 2. Calculations were based on formulae given by Horak (1950). In both

cases, analytical expressions could be derived. Specifically, we have

$$p(\Theta) = \frac{8}{3\pi} \left\{ \sin \Theta \cdot \cos^2 \Theta - \Theta \cdot \cos \Theta + \sin^3 \Theta \right\}, \quad k=1 \quad (12)$$

and

$$p(\Theta) = \frac{3}{4} \left\{ 1 - \cos \Theta \right\}^2, \quad k=2 \quad (13)$$

Both scattering phase functions are shown in Fig. 3. For comparison, relevant Henyey-Greenstein functions are also shown. Evidently, the scattering phase function for snowballs can be adequately described by the Henyey-Greenstein function with the anisotropy parameter in the range $-0.30 \leq g \leq -0.35$.

Low albedos, with very pronounced back-scattering, are also permitted by the analysis. Examples of astronomical bodies known to have such scattering properties are the Moon and Mercury. Like information for other astronomical bodies is not yet complete. Data on the Bond albedo of the Moon and on the lunar phase function are readily available (Allen, 1963). Mercury and the Moon are very similar. The lunar albedo is 0.068. The lunar phase function, normalized according to equation (1), is shown in Fig. 4. For comparison, relevant Henyey-Greenstein phase functions are also shown. The lunar phase function can be adequately described by the Henyey-Greenstein phase function with the anisotropy parameter in the range $-0.55 \leq g \leq -0.5$.

Results of the analysis, and comparisons with candidate ring particles, are summarized in Fig. 5. The g - ω envelope permitted by optical thicknesses in the range $0.5 \leq \tau \leq \infty$ is shown. In accordance with the earlier discussion, the calculations are based on adopted values for the primary-to-multiple scattering ratio relevant to the optical thickness selected, and to the special case x equal -1. For τ equal 0.5, maximum ω values are obtained by selecting $\frac{I}{F}$ equal 0.4 in equation (11); for τ equal infinity, minimum ω values are obtained using $\frac{I}{F}$ equal 0.25. Once again, analysis of the infrared thermal measurements (Price, 1976) is used to exclude single scattering albedos greater than 0.75. For comparison, the cases of snowballs and of the Moon are also plotted.

Evidently, ring particles with lunar-like scattering properties are excluded by the analysis. Their single scattering albedos would be too small for the permitted back-scattering efficiency or vice versa. Note that for anisotropy parameters g less than -0.25, the selected primary-to-multiple scattering ratios are necessarily less than actual. Bear in mind that for divert back-scattering, the ratio is always unity. Consequently, for the cases considered in Fig. 5, the single scattering albedos are too small by from zero up to 15-24 percent, depending on the degree of anisotropy. In reality, therefore, the difficulty in reconciling lunar-like ring particles with the analysis of the photometric function data is even greater than it appears in

Fig. 5. Even if the lunar albedo were increased by a factor 3 to reproduce the probable values for the most reflective asteroids (Chapman, 1976), reconciliation with the analysis would still be extremely difficult. Most likely, an increase in reflectivity would cause a decrease in back-scattering directivity (Oetking, 1966).

Interestingly enough, snowballs encounter no such difficulty. Pure spherical particles are in excellent agreement with the analysis. Even significant impurities in the snow will not lead to a discrepancy. Veverka (1973) has discussed qualitatively the effects of impurities. Two kinds of contaminants are possible. First, impurities which do not hinder multiple scattering within the surface snow layer to any appreciable degree may be present. Examples are frosts of CO_2 , CH_4 , NH_3 , etc. Second, impurities which effectively prevent multiple scattering may be present. These will radically alter the photometric properties of a snowball. Most mineral contaminants fall into the latter category. On the basis of preliminary laboratory studies, Veverka (1976) has suggested that the introduction of significant mineral contaminants would significantly decrease the single scattering albedo of snowballs, while increasing their back-scattering directivity. Both effects will cause movement of the "snowball" ω -g envelope in Fig. 5 towards smaller ω -values and more negative g-values. It is difficult to imagine how even heavily contaminated snowballs could move outside the ω -g envelope permitted by the photometric analysis.

Lebofsky, Johnson, and McCord (1970) have studied the visual reflection spectrum of Saturn's rings in detail. Either pure water frost, or silicate, particles are inconsistent with the measurements. Part frost-covered silicates and mixtures of frosts with other compounds, perhaps modified by ultraviolet or high-energy particles, are possible ring constituents. Our photometric analysis is consistent with their conclusions. Most probably, the ring particles are more-or-less pure and spherical conglomerates of predominantly H_2O frost.

ACKNOWLEDGMENTS

This research was supported by the National Aeronautics and Space Administration under Contract NASW-2853.

ORIGINAL PAGE IS
OF POOR QUALITY

REFERENCES

- Allen, C. W. (1963) "Astrophysical Quantities," Second Edition
(Athlone: London).
- Chandrasekhar, S. (1960) "Radiative Transfer" (Dover: New York).
- Chapman, C. R. (1976) Private Communication.
- Heney, L. G. and Greenstein, J. L. (1941) "Diffuse Radiation in
the Galaxy," *Astrophysical J.* 93, 70.
- Horak, H. G. (1950) "Diffuse Reflection by Planetary Atmospheres,"
Astrophysical J. 112, 445.
- Lebofsky, L. A., Johnson, T. V., and McCord, T. B. (1970)
"Saturn's Rings: Spectral Reflectivity and Compositional
Implications," *Icarus* 13, 226.
- Oetking, P. (1966) "Photometric Studies of Diffusely Reflecting Surfaces
with Applications to the Brightness of the Moon," *J. Geophys.*
Res. 71, 2505.
- Pollack, J. B. (1975) "The Rings of Saturn," *Space Sci. Rev.* 18, 3.
- Price, M. J. (1973) "Optical Scattering Properties of Saturn's Ring,"
Astronomical J. 78, 113.
- Price, M. J. (1974) "Optical Scattering Properties of Saturn's Ring, II,"
Icarus 23, 388.
- Price, M. J. (1976) "Infrared Thermal Models for Saturn's Ring,"
Icarus (In press).

Veverka, J. (1973) "The Photometric Properties of Natural Snow
and of Snow-Covered Planets," Icarus 20, 304.

Veverka, J..(1976) Private Communication.

FIGURE CAPTIONS

- Fig. 1 Special phase functions, for which analytical radiative transfer solutions exist, are described by the anisotropy parameter, x . Relevant Henyey-Greenstein functions, with anisotropy parameter, g , are shown for comparison.
- Fig. 2 Combinations of single scattering albedo, ω , and anisotropy parameter, g , permitted by the visual photometric function for Saturn's rings, for various selected ranges in the optical thickness, τ . See text for computational details. Shaded regions are excluded by the analysis; unshaded regions are permitted.
- Fig. 3 Scattering phase functions for snowballs, characterized by the Minnaert constant, k , equal 1 and 2, are compared with relevant Henyey-Greenstein functions, with anisotropy parameter, g .
- Fig. 4 Lunar phase function compared with relevant Henyey-Greenstein functions with anisotropy parameter, g .
- Fig. 5 Combinations of single scattering albedo, ω , and anisotropy parameter, g , permitted by the visual photometric function for Saturn's rings, for optical thicknesses in the range

$0.5 \leq \tau \leq \infty$. Regions labelled N/A are excluded by the analysis. See text for computational details. For comparison, the scattering parameters of the Moon, and of H_2O snowballs, are also plotted.

ORIGINAL PAGE IS
OF POOR QUALITY

APPENDIX B

LIMB-BRIGHTENING
ON URANUS:
THE VISIBLE SPECTRUM

by

Michael J. Price
Planetary Science Institute
Tucson, Arizona 85719

and

Otto G. Franz
Lowell Observatory
Flagstaff, Arizona 86001

Received _____

Revised _____

No. of Copies: 3

No. of MS Pages: 25

No. of Figures: 5

No. of Tables: 4

Proposed Running Head:

LIMB-BRIGHTENING ON URANUS

Name and Address of Person to Whom Proofs Should be Sent:

Dr. Michael J. Price
Planetary Science Institute
2030 E. Speedway Blvd., Suite 201
Tucson, Arizona 85719

ABSTRACT

Multi-color ($\lambda 5500\text{\AA}$ - $\lambda 7600\text{\AA}$), narrow-band (100\AA), area-scanning photometry has been used to study the wavelength variation in the optical appearance of Uranus. Limb-brightening has been detected in two CH_4 bands i.e. $\lambda 6190\text{\AA}$ and $\lambda 7300\text{\AA}$.

ORIGINAL PAGE IS
OF POOR QUALITY

1. INTRODUCTION

Belton and Vesculus (1975) have recently reviewed the UV-IR appearance of Uranus in the context of current knowledge regarding its atmospheric structure. Within a predominantly $H_2 - CH_4$ atmosphere, the tops of a thick NH_3 cloud layer should exist near the 3-4 bar level; there is also a very uncertain possibility of a thin, broken, CH_4 cloud layer near 300 mbars. But whether in fact the Uranus atmosphere is so structured remains very much an open question. Two major questions are of paramount interest:

1. Does the deep-dense NH_3 cloud layer really exist? Is it in fact observable? If so, at what pressure level is the top located?
2. Is the $H_2 - CH_4$ atmosphere above the NH_3 cloud layer perfectly clear? If not, what is the precise nature of the aerosol haze?

Answers may be obtained by imaging the planet from a fly-by spacecraft. But, until a Uranus mission is successfully accomplished, further knowledge of the planet must come from Earth- or Satellite-based observations.

Belton and Price (1973) have developed a straightforward test of the hypothesis that clouds are absent from the visible atmosphere of Uranus. Based on a clear, semi-infinite, pure $H_2 - CH_4$ gaseous model, it consists of measuring the wavelengths at which the character of the center-to-limb-intensity profile changes from limb-darkening to limb-brightening, and

vice versa. Limb-brightening occurs in certain wavelength regions by virtue of the vertical inhomogeneity in the atmosphere which results from pressure-related opacity sources. Where the dominant opacity is due to pressure-induced and pressure-broadened transitions in H_2 and CH_4 , the intensity profile of the Uranus disk changes character at a geometrical albedo of 0.23. Seven changeover wavelengths ($\pm 20\text{\AA}$) were predicted viz., 6120 \AA , 6240 \AA ; 6620 \AA , 6710 \AA ; 6970 \AA , 7420 \AA ; 7600 \AA . All of the deep CH_4 bands beyond 7600 \AA should be limb-brightened, as should the central regions of the CH_4 bands at 6190 \AA and 7300 \AA . Fig. 1 summarizes the Belton and Price (1973) predictions. Available observations, discussed below, were found to be in qualitative agreement with the model. But, they were not yet numerous enough, nor sufficiently accurate, nor made in the critical spectral regions to be conclusive.

For visual wavelengths (3800 \AA - 5800 \AA), Danielson, Tomasko, and Savage (1972) obtained a high-resolution composite image of Uranus. By using Stratoscope II, they were able to achieve a Gaussian point spread function with a half-intensity width 0.2 arc. Except for the presence of pronounced symmetrical limb-darkening, no certain disk markings were visible. Any faint belts parallel to the rotational equator must have a maximum contrast of 5 percent. The measured limb-darkening did not agree with either a deep Rayleigh atmosphere or with clouds high in the atmosphere; a cloud deck underlying a finite Rayleigh atmosphere seemed to be indicated. Light and Danielson (1973) found later that an H_2

ORIGINAL PAGE IS
OF POOR QUALITY

atmosphere, 400 km amagats deep, overlying a thick cloud would explain the Stratoscope II pictures. Although the Stratoscope II imagery shows no structural detail on the disk, the lack may simply be the result of low contrast introduced by the exceptionally wide band-width.

At infrared wavelengths, Westphal (1972) obtained two photoelectric scans across the Uranus disk in the passbands $8000\text{\AA} - 8240\text{\AA}$ and $8720\text{\AA} - 8960\text{\AA}$. Both were obtained simultaneously on 1971 March 8. The atmospheric seeing was $\sim 0.5''$ arc, and a circular $1''$ arc aperture was used. One scan ($8720\text{\AA} - 8960\text{\AA}$) has since been reproduced in the literature (Belton and Vesculus, 1975), but the other remains unpublished. The long wavelength scan is limb-brightened; the short wavelength scan shows a flat central region $\sim 2''$ arc wide together with limb-darkening. Also, the 8840\AA scan is asymmetric; the west limb appears brighter than the east limb. Investigation of the importance of smearing effects, due to the natural aperture response of the instrument and atmospheric seeing, showed that the tiny ($4''$ arc) disk of Uranus may appear limb-darkened even if weak limb-brightening is present. Taking spatial smearing into account, Belton and Price (1973) found no obvious contradictions between their predictions and the Westphal observations.

Infrared limb-brightening was confirmed by Sinton (1972). Several photographs of Uranus were obtained with a Varo-tube and an 8870\AA interference filter (140\AA half-width; 220\AA tenth width) under good seeing conditions ($\sim 1.1''$ arc). Both limb-brightening and polar brightening were found. Sinton interpreted the polar brightening in terms of a haze in the upper atmosphere, in addition to Rayleigh scattering. Unfortunately,

knowledge of the point spread function was too imprecise to permit detailed quantitative comparison with the Belton and Price (1973) predictions.

In their critical review of the visual, photoelectric, and photographic data, Belton and Vesculus (1975) concluded that markings do frequently occur on Uranus. But knowledge of the optical appearance of Uranus is still extraordinarily vague. Thoroughly defining the limitations of the semi-infinite, clear $H_2 - CH_4$ atmospheric model would be a significant step forward. Results of a systematic attempt to investigate in detail the validity of the Belton and Price (1973) predictions are reported in this paper.

2. OBSERVATIONS

Uranus is difficult to observe. Being located so far from the sun, the planet exhibits only a faint ($m_V \sim +6$), tiny ($\sim 4''$ arc diameter), disk. Atmospheric seeing broadening, typically $1'' - 2''$ arc, severely distorts the telescopic image. Detecting limb-brightening on Uranus is an extremely challenging problem. Fortuitously, photometry of close double stars encounters similar observational difficulties which, to a large extent, can be overcome by use of a photoelectric area-scanning technique. Pioneering development was carried out by Rakos (1965). Initial results were so promising that a scanner designed specifically for the simultaneous astrometric and photometric study of visual binaries was constructed (Franz, 1966; 1970). With minor modifications, the equipment was found to be eminently suitable for the Uranus task when mounted at the Cassegrain focus of the 72-inch aperture Perkins telescope at Lowell Observatory.

Exploring the nature of the Uranus disk profile as a function of geometrical albedo required the selection of eight narrow waveband ($\sim 100\text{\AA}$) filters spread throughout the region $\lambda 5500\text{\AA} - \lambda 7600\text{\AA}$ (Fig. 1). Characteristics of the filters are listed in Table I. Experience showed that choosing significantly narrower band widths would lead to inadequate signal/noise ratios at the longer wavelengths. To maximize the signal/noise ratio throughout, an EMI 9558 (S-20) photomultiplier was employed in the system.

Selecting the optimum technique for scanning across the Uranus disk required careful consideration. Use of a pinhole aperture is one option. With excellent seeing, the sensitivity to limb-brightening is maximized. But two significant problems appear under typical observing conditions. First, it is difficult to insure that a pinhole moves precisely across a diameter of the Uranus disk. If not, asymmetries in the scan may result. Second, theoretical interpretation of the data is extremely difficult even if the point spread function is reliably known. Determining the instrumental response for a finite circular aperture passing across a circular disk which contains a radial intensity gradient is a non-trivial exercise. By comparison, slit scans greatly simplify both the observational procedure and the data interpretation. If the slit length is significantly greater than the image diameter, radially symmetric scans are always assured. It is no longer essential for the aperture center to pass precisely through the image center. Specifically, accurate determination of the point spread function is readily achieved. Moreover, chord integration with slit broadening for either Uranus or a stellar image is a tractable analytical problem.

TABLE I
FILTER SET

Filter No.	Central Wavelength (\AA)
1	5600
2	6000
3	6200
4	6400
5	6800
6	7000
7	7300
8	7500

Notes: 1. Filters No. 1 - No. 6 inclusive were manufactured by the Optical Coating Laboratory. Tolerances in their central wavelengths are $\pm 30\text{\AA}$. In each case, the half-power band width (HPBW) is $100 \pm 20\text{\AA}$.

Peak transmission is a nominal 50%. Typical transmission figures are, 10% at 1.25 HPBW; 1% at 1.8 HPBW; 0.1% at 3.0 HPBW; $< 0.1\%$ at > 3.0 HPBW.

2. Filters No. 7 and No. 8 were manufactured by Infrared Industries, Thin Film Products Division. Tolerances in their central wavelengths are $\pm 15\text{\AA}$. In both cases, the half-power band width (HPBW) is $100 \pm 15\text{\AA}$. Peak transmission is a nominal 50%.

Both pinhole and slit scans were used in the observational program. Characteristic widths of the pinhole and slit were both chosen equal to 100μ ($0''.645$ arc). Wider apertures caused inadequate spatial resolution. Narrower apertures gave a poor signal/noise ratio throughout the wavelength range under study. Scan orientations were either north-south or east-west. NS scans were preferred; image broadening, through telescope drive error, could not occur. For EW scans, individual filter integration times were kept correspondingly short. Table II gives the complete Uranus observing log.

3. RESULTS

3.1. Coarse Analysis

Expeditious processing of the Uranus data required a simple, objective, method for detecting the coarsest features of the true intensity profile of the disk. Whenever seeing broadening is significant, limb-brightening on Uranus will manifest itself by a general widening of the planetary image. Similarly, limb-darkening will cause a relative image-narrowing. All observational data were acquired under ordinary Flagstaff atmospheric seeing conditions, stellar image diameters (half-power) being typically $\sim 2''$ arc. Both pinhole- and slit-scans of Uranus in all wavebands showed a characteristic Gaussian shape. Determining the Gaussian $1/e$ -width of the Uranus image in each waveband should therefore provide a reliable method for comparing relative limb-darkening/limb-brightening effects.

Coarse analysis of the observations consisted of determining, by the least squares technique, the Gaussian $1/e$ -width for each and every integrated

TABLE II
URANUS OBSERVING LOG

DATE(U.T.)	SCAN TYPE	FILTERS	SKY		REMARKS
			TRANSPARENCY	SEEING	
1974 May 1	P	1, 2, 3, 4, 5, 6, 8	5	2-3	E↔W
1974 May 26	P	1, 2, 3, 4	5	3-4	N↔S
1974 June 5	P	2, 3, 4	4	2	N↔S
1975 May 24	S	1, 2, 3, 4, 5, 6, 7, 8	4-5	3-4	N↔S; Scale known but no PSF information
1975 May 27	S	1, 2, 3, 4, 5, 6, 7, 8	5-3	3-2	N↔S; E↔W; Scale from ADS 9053; PSF from ζ Virginis
1975 June 15	S	1, 2, 3, 4, 5, 6, 7, 8	5	3	E↔W; Scale known; PSF from κ & ι Virginis
1975 June 16	S	1, 2, 3, 4, 5, 6, 7, 8	5	3	E↔W; Scale known; PSF from ι Virginis
1975 June 16	P	6, 7, 8	5	3	E↔W
1975 June 17	P	1, 2, 3, 4, 6, 7, 8	5	3	N↔S
1975 June 19	P	2, 3, 7, 8	5	3	E↔W

- Notes: 1. Scan type is either pinhole (P) or slit (S)
2. Filter No.'s are taken from Table I
3. Sky transparency and seeing conditions are each given on a scale 0-5 (i.e. Worst-Best)
4. Information concerning scale calibration and seeing data are given in the Remarks column.

pinhole- and slit-scan. Subsequent numerical experiments showed that the use of more sophisticated profile shapes had a negligible effect on the results cf: Franz et al (1971) and Franz (1973). Data secured using different scan-types and scan-orientations were initially kept segregated to determine if the results were sensitive to the mode of observation. Specifically, data taken on a particular night, by a particular scan technique, were treated as a complete set. Each set was obtained by a rapid, symmetrical, forward-backward cycling of the filter wheel. Integration times for each filter were normally in the range 20 - 500 seconds. For all observations within a given set, the seeing and transparency could be taken as constant. Detailed point spread function information, and accurate linear scale calibrations, were not always available on each night. Consequently, only relative profile widths were determined within each set; all profiles were conveniently normalized to the mean for Filter No. 2 ($\lambda 6000\text{\AA}$). Relative Gaussian profile widths are listed in Table III. The rms error of the individual relative width determinations are also shown. Where no rms error is available due to insufficient data, the uncertainty is indicated by a question mark. In parentheses, following each rms error, is the number of individual width determinations from which the mean value was calculated.

Table IV summarizes the results obtained from each combination of scan-type and scan-orientation. Corresponding mean values for the relative Gaussian widths have been derived from the values listed in Table III. Individual rms errors quoted in Table IV are based on the spread of the

ORIGINAL PAGE IS
OF POOR QUALITY

TABLE III
URANUS DISK: RELATIVE GAUSSIAN PROFILE WIDTHS

FILTER NO. DATE(U.T.)	1	2	3	4	5	6	7	8
<u>Pinhole Scans(N↔S)</u>								
1974 May 26	1.01 ₊ ? (1)	1.00 ₊ .02(3)	1.06 ₊ .02(2)	1.00 ₊ ? (1)	x	x	x	x
1974 June 5*	x	1.00 ₊ .00(3)	1.02 ₊ .01(3)	0.99 ₊ .01(3)	x	x	x	x
	x	1.00 ₊ .02(13)	1.04 ₊ .03(14)	0.98 ₊ .03(12)	x	x	x	x
1975 June 17	0.99 ₊ ? (1)	1.00 ₊ .03(4)	1.03 ₊ .03(5)	1.04 ₊ .03(2)	x	1.01 ₊ ? (1)	1.15 ₊ .02(2)	1.01 ₊ ? (1)
<u>Pinhole Scans(E↔W)</u>								
1974 May 1 ⁺	0.98 ₊ .02(3)	1.00 ₊ .03(6)	1.03 ₊ .03(7)	1.02 ₊ .04(5)	1.04 ₊ .03(3)	1.05 ₊ .01(3)	x	1.04 ₊ .01(2)
	1.01 ₊ ? (1)	1.00 ₊ .01(4)	1.04 ₊ .02(8)	1.00 ₊ .02(4)	1.00 ₊ ? (1)	0.99 ₊ ? (1)	x	x
1975 June 16	x	x	x	x	x	1.00 ₊ .02(2)	1.28 ₊ ? (1)	1.01 ₊ ? (1)
1975 June 19	x	1.00 ₊ .06(6)	0.99 ₊ .06(4)	x	x	x	1.06 ₊ ? (1)	0.89 ₊ ? (1)
<u>Slit Scans(N↔S)</u>								
1975 May 24	1.02 ₊ .01(2)	1.00 ₊ .00(2)	1.03 ₊ .00(2)	0.98 ₊ .01(2)	1.00 ₊ .00(2)	0.99 ₊ .01(3)	1.08 ₊ .02(4)	0.98 ₊ .01(2)
1975 May 27	0.99 ₊ .01(2)	1.00 ₊ .00(2)	1.02 ₊ .01(2)	0.99 ₊ .01(2)	0.96 ₊ .01(2)	0.95 ₊ .00(2)	1.05 ₊ .01(2)	0.97 ₊ .01(2)
<u>Slit Scans(E↔W)</u>								
1975 May 27	0.96 ₊ .00(2)	1.00 ₊ .01(2)	1.00 ₊ .03(2)	0.97 ₊ .02(2)	0.95 ₊ .03(2)	0.97 ₊ .03(2)	1.07 ₊ .01(2)	0.95 ₊ .02(2)
1975 June 15	1.04 ₊ .03(3)	1.00 ₊ .06(4)	1.03 ₊ .03(4)	1.02 ₊ .04(5)	1.02 ₊ .06(4)	1.01 ₊ .03(4)	1.08 ₊ .03(4)	1.01 ₊ .01(5)
1975 June 16	0.99 ₊ .01(2)	1.00 ₊ .01(2)	1.02 ₊ .01(2)	1.04 ₊ .03(2)	1.02 ₊ .02(2)	1.03 ₊ .02(4)	1.08 ₊ .01(2)	0.99 ₊ .01(2)

Notes: * Scale change between two sets of measurements

+ Cam change between two sets of measurements

TABLE IV

URANUS DISK: GAUSSIAN WIDTHS' SUMMARY

FILTER NO. DATE(U.T.)	1	2	3	4	5	6	7	8
Pinhole (N↔S)	1.00 _{±.01}	1.00	1.04 _{±.02}	1.00 _{±.02}	x	1.01 _{±?}	1.15 _{±.01}	1.01 _{±?}
Pinhole (E↔W)	1.00 _{±.02}	1.00	1.02 _{±.02}	1.01 _{±.01}	1.02 _{±.02}	1.01 _{±.03}	1.17 _{±.11}	0.98 _{±.06}
Slit (N↔S)	1.01 _{±.02}	1.00	1.03 _{±.01}	0.99 _{±.01}	0.98 _{±.02}	0.97 _{±.02}	1.07 _{±.02}	0.98 _{±.01}
Slit (E↔W)	1.00 _{±.03}	1.00	1.02 _{±.01}	1.01 _{±.03}	1.00 _{±.03}	1.00 _{±.03}	1.08 _{±.01}	0.98 _{±.03}
Mean	1.00 _{±.01}	1.00	1.03 _{±.01}	1.00 _{±.01}	1.00 _{±.01}	1.00 _{±.02}	1.12 _{±.04}	0.99 _{±.01}

Notes: 1. Each type of scan data is normalized to Filter No. 2

2. If no rms error is available through insufficient data, the uncertainty is indicated by a question mark.

relevant values listed in Table III. Throughout, all mean relative Gaussian widths have been normalized to Filter No. 2. For each filter, a final relative Gaussian width has also been derived by averaging the values listed in Table IV itself. The corresponding rms error has been obtained from the actual spread in the Table IV numbers. Several conclusions can be drawn:

1. Except for Filters No. 3 and No. 7, there is no evidence of any change in the Gaussian $1/e$ width of the Uranus image with wavelength.
2. Filters No. 3 and No. 7 both show evidence of an increase in the Gaussian $1/e$ width relative to Filter No. 2. Moreover, the increase is larger for Filter No. 7 than for Filter No. 3.
3. For Filter No. 7, the relative Gaussian $1/e$ width is significantly larger if pinhole-scanning rather than slit-scanning is employed.
4. Scan-orientation does not significantly affect the relative Gaussian $1/e$ widths. Evidently, the telescope guiding was accurate.

Our results are most readily explained by the presence of limb-brightening in the wavebands corresponding to Filters No. 3 and No. 7. Moreover, the limb-brightening should be more pronounced for Filter No. 7 than for Filter No. 3.

Composite pinhole NS scans were constructed to maximize the visibility of limb-brightening on the Uranus disk. Specimen results are illustrated in Fig. 2. Observations taken on 1975 June 17 were selected on the basis

of stability both in the atmospheric seeing quality and in the sky transparency, Filter No. 7 corresponds to the deep $\lambda 7300\text{\AA}$ CH_4 band in which limb-brightening is to be expected. Filters No. 6 and No. 8 refer to adjacent wavelengths in which limb-brightening is not anticipated. The Filter No. 7 profile was constructed by summing two integrated scans made up of 1000 and 500 individual one-second scans respectively. Integrated scans, each made up of 200 individual scans were used to form the composite of filters No. 6 and No. 8. Gaussian curve-fitting parameters were used in the co-location, background elimination, and normalization, of the integrated scans. For Uranus, the photodetector response for filters No. 6 and No. 8 was ~ 6 times greater than for filter No. 7. Significant differences in the signal/noise ratio are apparent in Fig. 2. A difference in the profile widths can be detected through inspection; Gaussian curve-fitting shows the filter No. 7 profile to be significantly wider cf: Table III.

3.2. Fine Analysis

Detailed quantitative studies of selected Uranus observational data were carried out to confirm and enhance the results of the coarse analysis. Attention was concentrated on the $\lambda 7300\text{\AA}$ CH_4 band where limb-brightening appeared to be most pronounced. Determining whether the apparent limb-brightening was in fact absolute, or merely relative, was of prime interest. Results obtained would have a direct bearing on the interpretation of the $\lambda 6190\text{\AA}$ CH_4 band data. Several criteria were used in the data selection.

First, stability in the observing conditions was of paramount importance. Not only must the sky transparency be uniformly excellent, to maximize

photometric accuracy, but the atmospheric seeing must be exceptionally stable. While excellent seeing would have been ideal, constancy rather than narrowness was the watchword for the point spread function. Second, accurate scale-calibration of the linear scan was essential. Third, slit-scans only could be utilized; quantitative interpretation of pinhole data was intractable. Fourth, since maximizing the limb-brightening/limb-darkening contrast was vital, composite profiles for Filter No. 7 and for Filters No. 6 and No. 8 were considered to be essential for detailed comparison. Their construction required the availability of significant numbers of integrated scans. Observations made on 1975 June 15 were found to be optimum cf. Tables II and III. Scan-orientation did not compromise the selection. NS- or EW-scans had been found to lead to essentially identical profiles.

Point spread function (PSF) data, in the relevant wavebands, were obtained from slit-scans of two stars, κ Vir and ι Vir, both near Uranus. To validate atmospheric seeing stability, the Uranus and stellar scans were intermingled. Eleven integrated stellar scans, taken through Filters No. 6 (3), No. 7 (4), and No. 8 (4), were used to derive a composite PSF profile relevant to the quantitative interpretation of the Uranus data (Fig. 3). No significant color-dependent differences in the shapes and widths of the stellar profiles were apparent. Each integrated stellar scan was uniformly comprised of 20 one-second sweeps. Gaussian curve-fitting parameters were used in the colocation, background elimination, mirror-imaging, and normalization, of the stellar data. The linear scale was determined using the visual

Binary 6 Ser (ADS 9701: Separation (1975.5) = $3.96 \pm 0.02''$ arc). Quantitatively, the atmospheric seeing stability can be described by the rms deviation of the eleven individual Gaussian $1/e$ -width parameters of the chosen stellar scans. An rms error of only 5.8 percent was derived.

Selected Uranus data comprised 13 integrated scans spread throughout the three wavebands in the following manner: Filter No. 6 (4), Filter No. 7 (4), and Filter No. 8 (5). Each Filter No. 6 scan consisted of 20 one-second sweeps. Three Filter No. 7 scans each consisted of 200 sweeps; a fourth scan was made up of 100 sweeps. Each Filter No. 8 scan consisted of 100 sweeps. Derived Gaussian $1/e$ -widths for all Filter No. 6 and Filter No. 8 integrated scans were statistically intercompared to determine if the selected waveband, or the number of individual sweeps within each scan, significantly affected profile shape. No indications of any such differences were found. A composite "continuum" profile was therefore derived by taking all Filter No. 6 and Filter No. 8 integrated scans together. For Filter No. 7, the number of sweeps making up each integrated scan did not affect the Gaussian $1/e$ -width. A composite $\lambda 7300\text{\AA}$ CH_4 band profile was therefore derived by taking all Filter No. 7 integrated scans together. Expeditious use was made of the Gaussian curve-fitting parameters to derive each composite Uranus profile. Special care was taken to insure that each composite scan was normalized at the precise center of the disk. Final normalization utilized data within 5 channels ($0''.15$ arc) radius of the disk center.

ORIGINAL PAGE IS
OF POOR QUALITY

The composite Uranus slit-scan profiles in the $\lambda 7300\text{\AA}$ CH_4 band, and in adjacent "continuum" regions, are compared in Figs. 4 and 5. Brief inspection of the observational data shows the CH_4 band profile to be significantly broader. Relative broadening is particularly noticable at distances 1-2 Uranus angular radii from the disk center. This is precisely where effects of limb-brightening would be expected to show to maximum advantage. Relative limb-brightening, first indicated by the coarse analysis, is confirmed.

Inferring the true intensity profiles of the Uranus disk can be based on either of two techniques. One may attempt to deconvolve the various smearing functions affecting each composite scan. Alternatively, numerical prediction of the observations, based on subjecting individual models of the true disk profile to various smearing mechanisms, may be used. For convenience, the numerical prediction technique was adopted. Three distinct models of the Uranus disk were considered. Model I represents a disk of uniform surface brightness. Model II assumes limb-brightening; the surface brightness varies linearly from zero at the disk center to a finite value at the limb. Model III assumes limb-darkening; the surface brightness varies linearly from a finite value at the disk center to zero at the limb. In modelling the Uranus disk, circular symmetry was adopted. From the results of Danielson, Tomasko, and Savage (1972), the Uranus radius was taken as 25,900 kms. Distance from the Earth to Uranus at the time of observation was taken from the 1975 American Ephemeris and Nautical Almanac to be 17.89 A.U. The corresponding angular diameter of Uranus (unbroadened) was therefore 3.99" arc.

Three distinct smearing mechanisms together affect the original Uranus disk to produce the observed planetary profile. First, every point on the disk is subjected to two-dimensional seeing broadening by a circularly symmetric point spread function. Second, chord-integration of the radially symmetric planetary image occurs because of the type of scan employed. Third, slit-broadening of the chord-integrated profile results from the need to use a finite scanning aperture. Chord-integration and slit-broadening both affect the original PSF shape to produce the observed slit scan of a stellar image. For convenience, the original PSF function was taken as Gaussian. Not only does a radially symmetric Gaussian profile provide an adequate first order description of the original point spread function, but its adoption leads to important mathematical simplifications in the theoretical convolution of the Uranus disk.

PSF observational data and theoretical predictions are compared in Fig. 3. Observational points refer to the composite slit-scan profile derived from individual stellar images. Theoretical predictions utilize the known slit width ($0''.645$ arc) together with individual selected values for the Gaussian $1/e$ -width (σ) of the original PSF. In keeping with the experiences of Franz et al (1971) and Franz (1973), no unique Gaussian curve provides a perfect fit to the observations. Nevertheless, limiting values for an effective Gaussian $1/e$ -width can be derived. By inspection of Fig. 3, it must lie in the range $1''.25 \leq \sigma \leq 1''.75$. Evidently, a narrower Gaussian curve is required in the core of the stellar image than in the wings. The optimum Gaussian $1/e$ -width (σ) was taken as $1''.5$ arc. Extreme error bars $\pm 0''.25$ arc were adopted.

ORIGINAL PAGE IS
OF POOR QUALITY

Determining the reality of absolute limb-brightening in the CH_4 band was the objective for the theoretical predictions shown in Fig. 4. Model I, a uniform circular disk, was selected to describe the unbroadened Uranus image. Detailed image convolution was carried out using three individual choices for the Gaussian 1/e-width (σ) of the original PSF i.e. 1".25, 1".5, and 1".75. In Fig. 4, the central curve refers to the intermediate Gaussian 1/e-width (1".5). CH_4 band observations lie significantly above the central curve, strongly indicating that the apparent limb-brightening is in fact absolute. Even if the widest permissible Gaussian 1/e-width is adopted (top curve), the Uranus disk must still be uniformly bright. If the narrowest PSF is adopted (lower curve), the need for absolute limb-brightening becomes very obvious. For the so-called continuum profile, use of the intermediate Gaussian 1/e-width strongly suggests that the unbroadened Uranus disk is uniform. Use of the widest PSF indicates limb-darkening; the narrowest PSF leads to limb-brightening.

Determining the sensitivity of the slit-scan profile to extreme variations in the original distribution of surface brightness on the Uranus disk was the objective of the theoretical predictions shown in Fig. 5. Three distinct intensity profiles were selected to describe the Uranus disk viz. Model I (Uniform disk), Model II (Extreme limb-brightening), and Model III (Extreme limb-darkening). In each case, the original PSF was defined by the intermediate Gaussian 1/e-width (1".5). In Fig. 5, Models I, II and III are represented by the middle, top, and lower curves respectively. Evidently, extreme limb-brightening must be present on Uranus in the $\lambda 7300\text{\AA}$ CH_4 band. If not, the

phenomenon would never have become apparent under the mediocre seeing conditions which existed during the course of the observations. Under better seeing conditions, limb-brightening should become very striking.

4. CONCLUSIONS

From our coarse analysis, the Uranus disk must exhibit limb-brightening in two CH_4 bands ($\lambda 6190\text{\AA}$; $\lambda 7300\text{\AA}$) relative to all other wavebands studied. Whether the apparent limb-brightening was in fact absolute, or only relative, could not be immediately determined. Except for the two CH_4 bands, the shapes and widths of the Uranus images were essentially identical. Since limb-darkening is known to occur at visual wavelengths ($\lambda 5600\text{\AA}$), it must occur in all so-called continuum wavebands studied. No systematic wavelength-dependent effects were found in the original point spread function which might have affected interwaveband comparisons. PSF data for all wavebands showed no significant variation in the representative Gaussian $1/e$ -width with wavelength.

From our fine analysis, absolute limb-brightening was found in the $\lambda 7300\text{\AA}$ CH_4 band. Taking into account results of the coarse analysis, absolute limb-darkening was found in the adjacent wavebands. No definite conclusions could be drawn regarding the absolute nature of limb-brightening in the $\lambda 6190\text{\AA}$ CH_4 band. If absolute limb-brightening does occur, it must be considerably less pronounced than in the $\lambda 7300\text{\AA}$ CH_4 band.

Although our results are consistent with the basic predictions of Belton and Price (1973), the validity of the $\text{H}_2 - \text{CH}_4$, semi-infinite, clear atmosphere remains to be proven. First, further observations secured under improved

ORIGINAL PAGE IS
OF POOR QUALITY

seeing conditions are required to better define the Uranus disk profiles. Second, alternative explanations of the limb-brightening phenomenon must be thoroughly evaluated. For instance, the observational consequences of a thin aerosol haze, located high in an otherwise clear $H_2 - CH_4$ atmosphere, require detailed prediction. Effects introduced by the presence of a deep dense NH_3 cloud layer must also be considered. Further observations and theoretical analyses are under way.

ACKNOWLEDGEMENTS

This research was supported by the National Aeronautics and Space Administration under contracts NASW-2521 and NASW-2718. Some of the data reductions were carried out with the support of NASA grant NGR-03-003-001. The equipment used to secure the observations was originally developed, assembled, and tested with the support of National Science Foundation grants GP-6983 and GP-20090. The Ohio State and Ohio Wesleyan Universities generously lent us an EMI 9558 photomultiplier for the project.

ORIGINAL PAGE IS
OF POOR QUALITY

REFERENCES

- Belton, M.J.S. and Price, M.J. (1973) "Limb-brightening on Uranus: A Prediction, *Astrophys. J.* 179, 965-970.
- Belton, M.J.S. and Vesculus, F.E. (1975) "Why Image Uranus?", *Icarus* 24, 299-310.
- Danielson, R.E., Tomasko, M.G., and Savage, B.D. (1972) "High-Resolution Imagery of Uranus Obtained by Stratoscope II", *Astrophysical J.* 178, 887-900.
- Franz, O.G. (1966) "Photometry and Astrometry of Close Double Stars", *Lowell Observatory Bulletin No. 134*, 6, 251-256.
- Franz, O.G. (1970) "A Photoelectric Area Scanner for Astrometry and Photometry of Visual Double Stars", *Lowell Observatory Bulletin No. 154*, 7, 191-197.
- Franz, O.G. (1973) "Observational Procedures for Visual Double-Star Work", *J. Roy. Ast. Soc. Canada* 67, 81-86.
- Franz, O.G., Millis, R.L., and White, N.M. (1971) "Photometry of Variables in Close Visual Double Stars" in *I.A.U. Colloquium No. 15 "New Directions and New Frontiers in Variable Star Research"*, Bamberg pp. 230-234.
- Light, E.S. and Danielson, R.E. (1973) Paper presented at the Fourth Annual Meeting of AAS Division of Planetary Sciences, Tucson, Arizona
- Rakos, K.D. (1965) "Photoelectric Area Scanner", *Applied Optics* 4, 1453-1456.
- Sinton, W.M. (1972) "Limb and Polar Brightening of Uranus at 8870Å," *Astrophys. J.* 176, L131.
- Westphal, J.A. (1972) Private Communication to M.J.S. Belton and M. J. Price.
- Younkin, R. L. (1970), Thesis, University of California, Los Angeles.

FIGURE CAPTIONS

Fig. 1. The schematic variation of the Uranus geometrical albedo, p , with wavelength, λ (after Younkin, 1970). The values of geometrical albedo given by Younkin have been adjusted to the radius derived by Danielson et al (1972). Limb-darkening is predicted to occur in the shaded regions; limb-brightening in the unshaded regions (Belton and Price, 1973). The multi-color filters employed in the observations are shown by the numbered bars. Approximate extremities in their transmission curves are indicated.

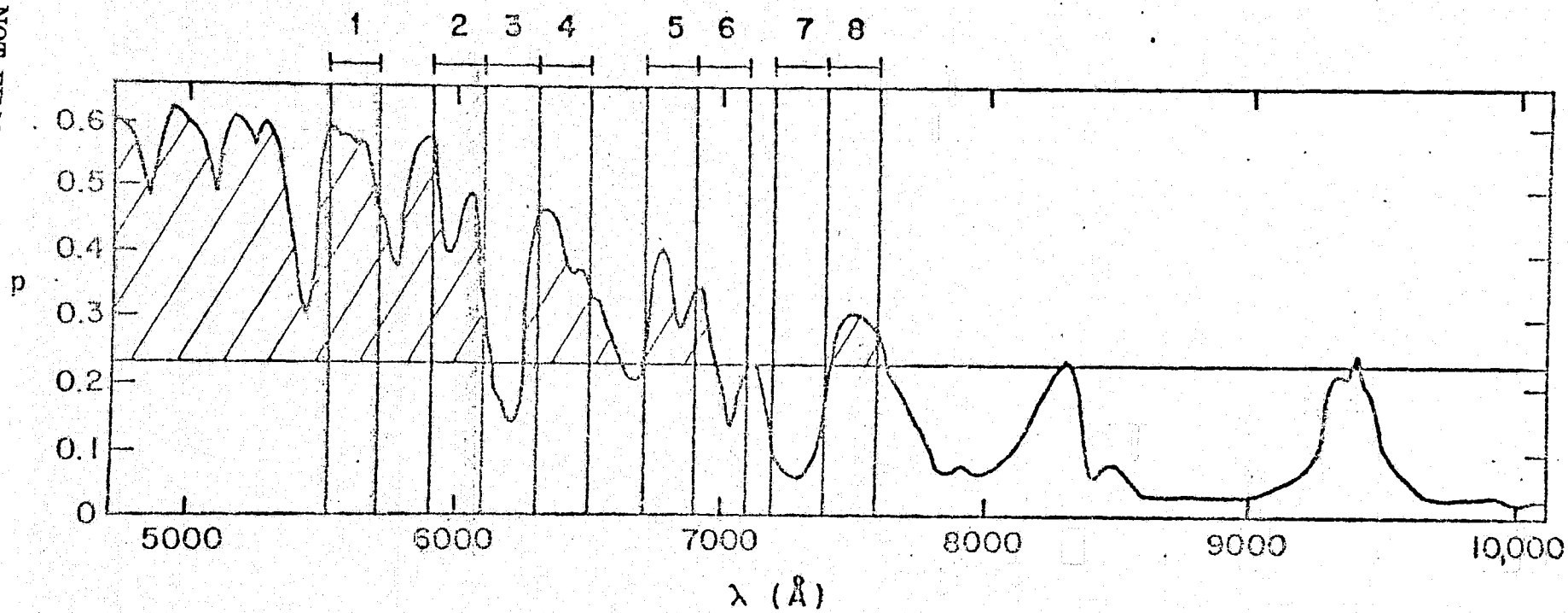
Fig. 2. Composite NS pinhole scans of Uranus obtained on 1975 June 17. Each point corresponds to a discrete channel of the linear scan.

Fig. 3. The Composite PSF slit-scan profile. Theoretical curves are based on individual choices for the original PSF Gaussian 1/e-width (σ). Slit width is 0".645 arc.

Fig. 4. The composite Uranus slit-scan profiles. Filter No. 7 (CH_4 band) and Filter No. 6/No. 8 (Continuum) data are plotted separately. Theoretical predictions refer to a uniform planetary disk. Individual choices for the original PSF Gaussian 1/e-width (σ) were 1".25, 1".5 and 1".75. The slit-width was 0".645 arc.

Fig. 5. The composite Uranus slit-scan profiles. Filter No. 7 (CH_4 band) and Filter No. 6/No. 8 (Continuum) data are plotted separately. Theoretical predictions refer to the intermediate original PSF Gaussian 1/e-width (1".5) coupled with individual choices for the planetary disk profile viz. Model I (Uniform Disk), Model II (Extreme limb-brightening) and Model III (Extreme limb-darkening). Slit-width was 0".645 arc.

PRECEDING PAGE BLANK NOT FILMED



1.0

FILTER 7

0

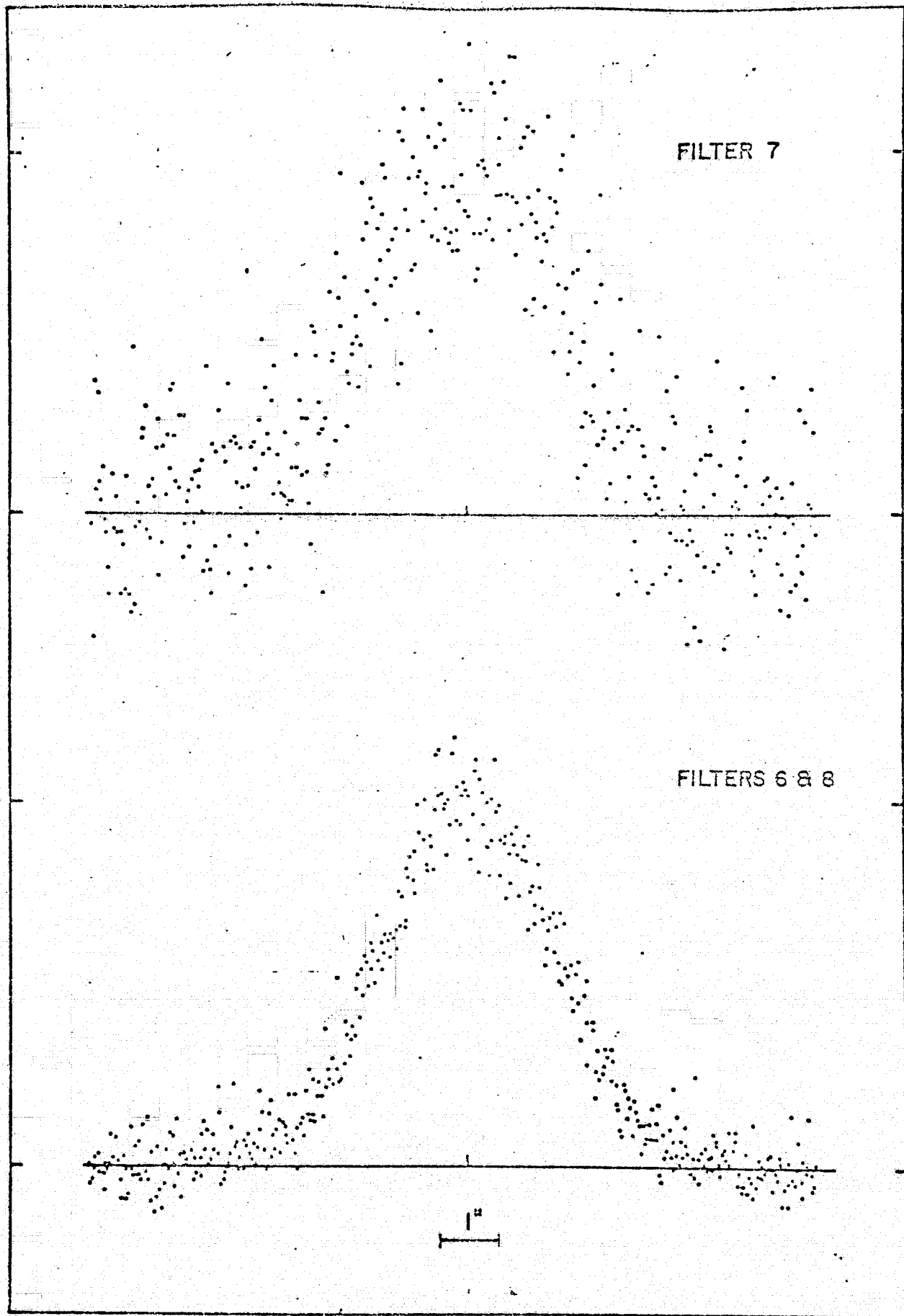
1.0

FILTERS 6 & 8

0

1^u

Fig 2



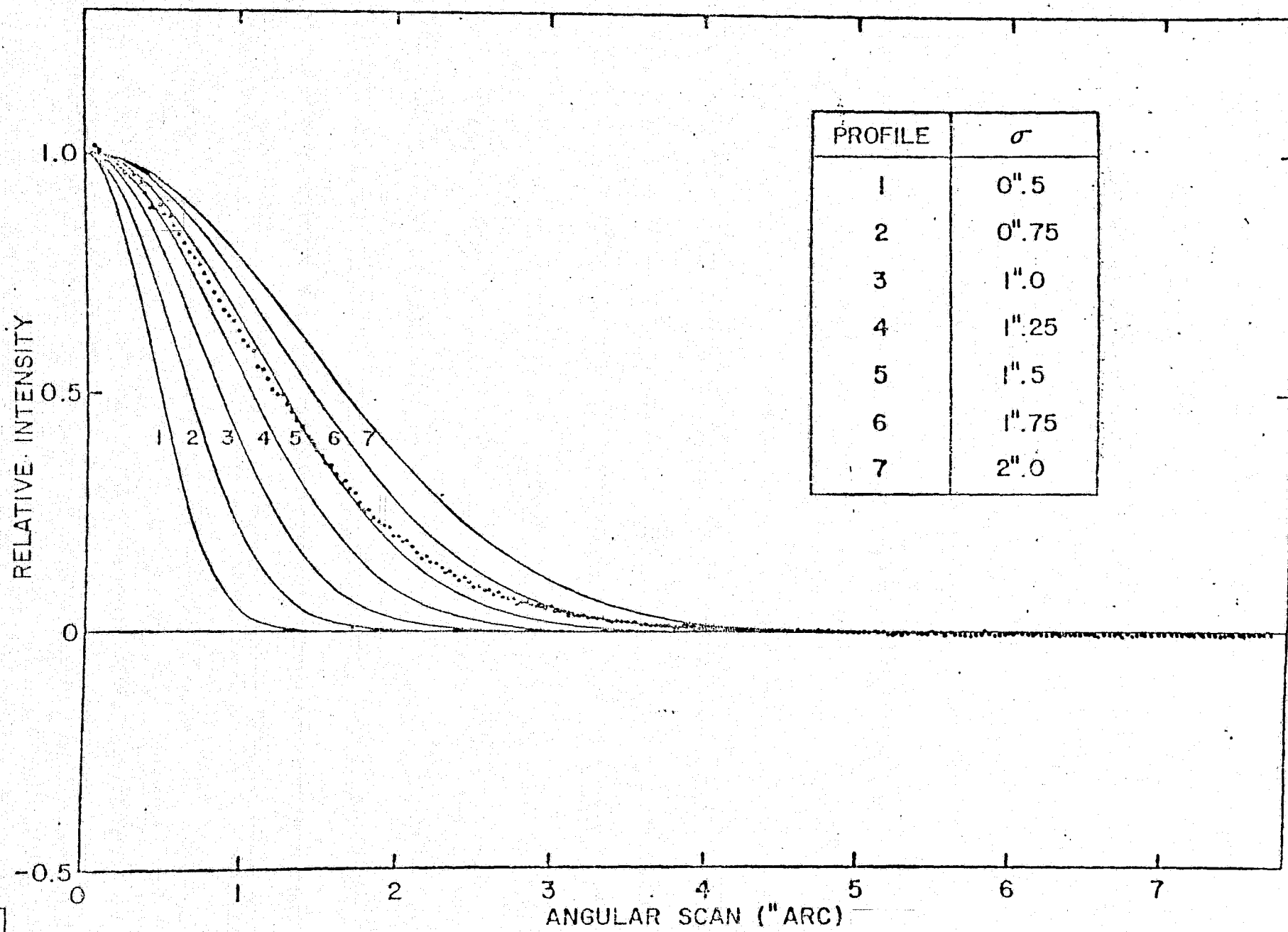


Fig. 3

URANUS ANGULAR RADII

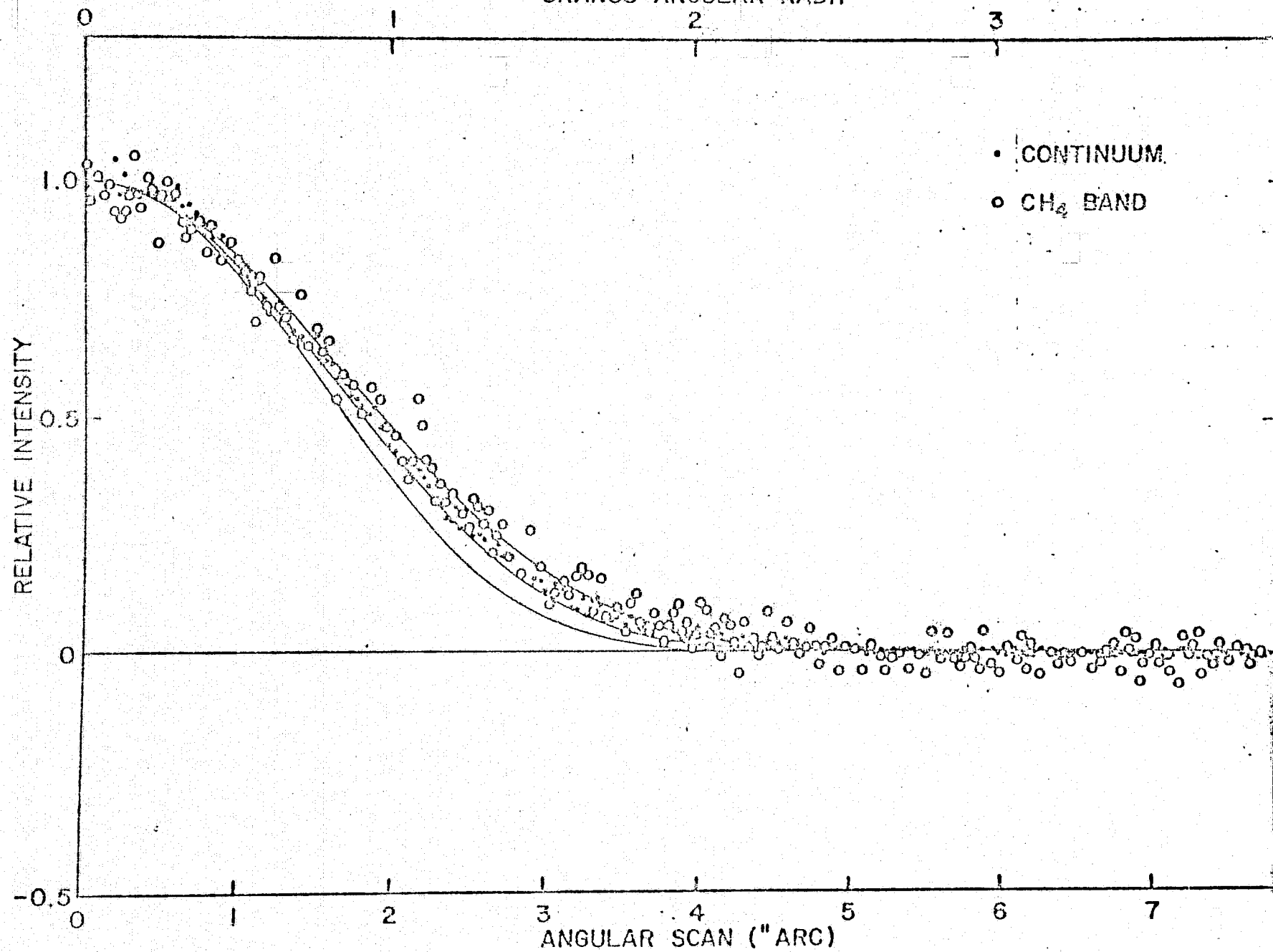


Fig. 4

URANUS-ANGULAR RADII

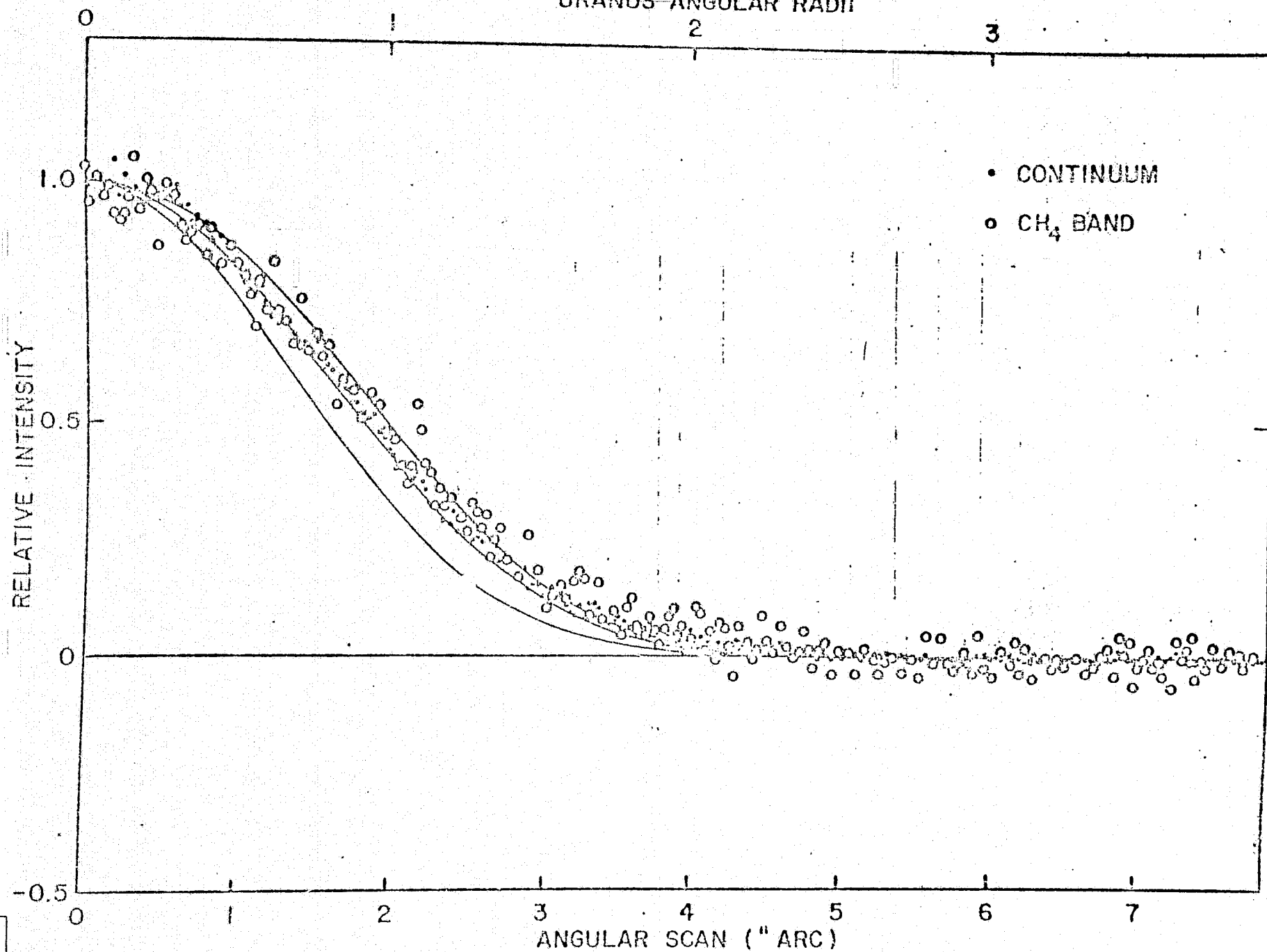


Fig. 5